batteries

Article

Numerical Analysis of Novel Air-Based Li-Ion Battery Thermal Management

Wei Chen [1], Shaobo Hou [1], Jialin Shi [1], Peng Han [1,*], Bin Liu [1], Baoping Wu [2] and Xiaoxiao Lin [2]

[1] School of Mechanical Engineering, Shijiazhuang Tiedao University, Shijiazhuang 050043, China
[2] CSSC No. 718 Research Institution, Handan 056000, China
* Correspondence: hp_128@126.com

Abstract: The lithium-ion battery is considered the primary power supply source for electric vehicles due to its high-energy density, long lifespan, and no memory effect. Its performance and safety highly depend on its operating temperature. Therefore, a battery thermal management system is necessary to ensure an electric vehicle (EV)'s performance. Air as a cooling medium is still used in a wide range of thermal management system applications, owing to its low-cost and lightweight. However, the conventional air-based cooling strategy shows an insufficient heat dissipation capacity and usually fails to block the thermal runaway propagation between batteries. Thus, it is of great importance for improving the heat dissipation of an air-based thermal management system. In this paper, three novel schemes (schemes B, C, and D) are introduced successively based on enhancing the heat transfer capacity and safety of a battery pack under a thermal runaway condition. Schemes B and C introduce a hollow spoiler prism and a spoiler prism filled with phase-change material with fins, respectively. The cooling effects of the three schemes are compared using computational fluid dynamics technology. The models of all the schemes are 3D symmetrical structures. In the CFD model, the battery heat-generating sub-model is incorporated through a user-defined function. The results indicate that all three schemes reduce the maximum temperature and the maximum temperature difference in the pack effectively compared with the conventional air cooling system. Scheme D presents the best cooling performance and hinders the propagation of the TR between adjacent batteries under a TR condition. The paper may provide a feasible method for improving the performance of an air-cooled thermal battery management system.

Keywords: thermal management; electric vehicle; thermal runaway propagation

check for updates

Citation: Chen, W.; Hou, S.; Shi, J.; Han, P.; Liu, B.; Wu, B.; Lin, X. Numerical Analysis of Novel Air-Based Li-Ion Battery Thermal Management. *Batteries* **2022**, *8*, 128. https://doi.org/10.3390/batteries8090128

Academic Editors: Quanqing Yu, Yonggang Liu and Xiaopeng Tang

Received: 31 July 2022
Accepted: 2 September 2022
Published: 17 September 2022

Publisher's Note: MDPI stays neutral with regard to jurisdictional claims in published maps and institutional affiliations.

Copyright: © 2022 by the authors. Licensee MDPI, Basel, Switzerland. This article is an open access article distributed under the terms and conditions of the Creative Commons Attribution (CC BY) license (https://creativecommons.org/licenses/by/4.0/).

1. Introduction

Under the background that the world is promoting the process of carbon peaking and carbon neutrality goals, the market share of electric vehicles (EVs) will irreversibly rise dramatically [1]. Batteries are considered one of the essential components of EVs. The lithium-ion (li-ion) battery is popularly used in EVs to date, owing to its feature of high-energy density, long lifespan, and no memory effect [2,3]. Usually, batteries form as modules first, then several modules form a pack. One pack is directly for one EV, and several packs might form a system for home or grid energy storage units. Batteries will generate heat when charging and discharging. When the heat is incapable of being timely carried from the batteries, the temperature will increase rapidly. The high temperature affects the battery performance and lifespan, and the local high temperature raises the temperature difference in the battery packs, which shortens the service life. Moreover, the accumulation of heat in one battery may trigger a series of exothermic chemical reactions, leading to an express increase in temperature and even thermal runaway (TR) [4]. When one of the batteries in the pack triggers a TR, if effective insulation cannot be carried out between the batteries, resulting in the propagation to other batteries, it will cause serious

consequences. Therefore, battery thermal managements systems (BTMSs) are required to dissipate the heat from the battery in time [5].

In the last decades, several types of BTMSs have been developed. Depending on the type of cooling medium, BTMSs can be categorized into four primary categories: an air cooling system (ACS) [6], a liquid cooling system [7], a phase-change-material (PCM) cooling system [8], and a heat pipe cooling system [9]. ACSs are widely applied for light-duty EVs equipped with small-scale battery packs, owing to its simple structure, light weight, and affordable price. However, an ACS usually fails to meet the heat dissipation requirement for heavy-duty EVs owing to the low convective heat transfer coefficient of air. An ACS is also accompanied by the issue of large temperature no-uniformity in the battery pack [10]. Furthermore, an ACS makes it difficult to prevent TR propagation. Many previous ACSs in the literature mainly focused on enhancing the heat transfer and reducing the energy consumption by increasing the turbulence and adjusting the battery layouts [11]. Park et al. [12] carried out a computational fluid dynamics (CFD) model to study the effects of battery layout on the cooling performance and energy consumption of an air-based BTMS. Kausthubharam et al. [13] numerically studied the performance of a forced ACS consisting of 36 batteries. The results illustrated that a forced ACS lowered the maximum temperature (Tmax) substantially, whereas it raised the temperature inhomogeneity. In addition, raising the inlet air velocity decreased the Tmax. In Li et al. [14], through experiments on the addition of silicon cooling plates and copper mesh on both sides of the bag pool battery, the results of the study showed that the protocol enhanced the heat transfer capacity of an air-based BTMS. In addition, the experiment also analyzed the effects of the wind speed, inlet position, and number of fans on heat transfer. Wang et al. [11] obtained the database of the uneven battery distances in the two directions in a pack between the performance of an ACS BTMS (Tmax and energy consumption) through a numerical simulation. Then, they established the relationship between the distance and performance through a BP neural network and optimized the distance. The performance after optimization was improved significantly. Liu et al. [15] proposed a novel J-type air-based battery thermal management system, taking advantage of a newly developed battery electrothermal model, and the grouped-channel optimizations were performed using surrogate-based optimization. The optimal results showed that there was a 31.18% reduction in the temperature rise for the J-type. Although the air-based BTMS has the dominant benefits mentioned above, the low convective heat transfer coefficient of air may make it difficult to meet the heat dissipation requirement. Furthermore, there have been few studies on using an ACS BTMS to prevent the TR propagation.

Nowadays, the liquid cooling technology is mainly chosen as the cooling technology for medium and high-end EV industrial applications. Liquid coolant has a relatively higher thermal conductivity and heat capacity, resulting in dissipating more heat under the same energy consumption, and is more appropriate for high-current or large-scale battery packs. Sheng et al. [16] proposed the structure of a liquid cooling fluid channel through numerical simulation and analyzed the influence of the channel size and cooling medium on the temperature distribution of a battery pack that consisted of 21,700 cylindrical batteries. The temperature rise and the temperature difference were, respectively, within 40 K and 5 K in the whole designed channel dimensions and cooling medium. For a liquid cooling BTMS, the current studies focused on improving the performance by developing the flow-channel layout and improving the thermal performance of the cooling liquid. The main drawback of a liquid cooling BTMS is that the structure tends to be complex and may be accompanied by a risk of leakage. Liquid cooling will also make extra weight for a pump and pipe connection, have high maintenance, and a high initial manufacturing cost [17]. In addition, due to the pressure of the entire cooling system, it will lead to an increase in energy consumption [2].

A BTMS using a PCM is one of the current research hotspots, which is on account of the highly absorbing massive heat when melting the PCM over a narrow temperature range. It decreases the Tmax and is cost-effective and reliable. Hallaj et al. [18] carried out the

research on a BTMS based on a PCM. It was found that the PCM significantly enhanced the temperature distribution in the pack during various discharge rates. Yan et al. [19] pointed out that the cooling capacity of the PCM system was better than that of the ACS system, especially when the discharge rate was relatively high. However, the PCM can only absorb heat passively. Thus, in some extreme conditions, available latent heat depletion may result in BTMS failure [20]. Considering the tradeoff between the capital cost for the PCM, fan power requirement, and variability in the heat rejection rate, the optimal quantity of the PCM and the maximum air velocity for the maximum current density of 260 mA/cm^2 (0.55 C-rate) were found to be 0.74 g/Wh and 3 m/s, respectively [21]. In addition, the thermal conductivity of PCMs tends to be low, which limits the commercial application of such a BTMS. At present, PCM is mainly in the laboratory stage. Some researchers suggested that the thermal conductivity of a PCM was able to be raised by combining with fins. Indicated in the article [22], the enhancement method, such as attaching fins on the surface of battery cells, is adopted in a PCM-based BTMS, enhancing the heat transfer due to the larger contact area. Ping et al. [23] designed a novel structure combing a PCM with fins to improve the BTMS performance. The BTMS of the LiFePO4 battery pack aimed to reduce the maximum temperature and improve the temperature uniformity in a high-temperature environment (40 °C). It found that the PCM with fins significantly decreased the Tmax and enhanced the temperature uniformity under a relatively high temperature condition. Jay R. Patel et al. [24] proposed that the low thermal conductivity of a PCM can be solved by increasing the surface area of the metal fins. Sun et al. [25] presented a novel BTMS which introduced longitudinal fins and cylindrical rings around the PCM. It was indicated that the novel BTMS exhibited a better performance compared with the pure PCM BTMS. In a word, the introduction of fins in the BTMS system is a very good scheme. The fins play a good role in the heat dissipation performance of the BTMS system, so the fins are introduced in this article to study the effect of the fins on the BMTS system.

The heat pipe is an innovative and efficient heat exchanger that can be cooled without an external power supply. In recent years, the research on heat pipes in BTMSs is increasing. Yi et al. [26] applied heat pipes to control the battery pack temperature. The results indicated that the Tmax was 313.15 K. The maximum temperature differences were 5 K. However, the heat pipe cooling system requires a heat sink and is usually combined with other cooling methods.

To compensate for the drawbacks of a single cooling system, BTMSs with two or more cooling methods have been reported in the last decades [27], a so called hybrid BTMS. Although increasing the costs and weight, this kind of BTMS considerably increases the temperature uniformity and significantly reduces the maximum temperature rise, because a hybrid BTMS benefits from the merits of different cooling methods. Ling et al. [28] studied the time-varying temperature profiles of a hybrid BTMS combined with a PCM and ACS cooling. It is indicated that the BTMS successfully decelerated the temperature rise, and the Tmax was below 323.15 K in all cases. Kizilel et al. [29] carried out a hybrid BTMS combined with an ACS with a composite PCM. It was found that the PCM assisted with the heat removal and helped in lowering the cell temperature with more cell-to-cell temperature uniformity. Wu et al. [30] studied the thermal behavior of lithium-ion batteries under natural convection conditions, forced convection, and heat pipe battery cooling systems by differentiating the state of charge and discharge current when discharging. They argue that forced convection has a higher cooling performance than natural convection, with the disadvantage of causing uneven temperature distribution, but their results show that the method of heat pipe cooling reduces the temperature by 32 °C, and its temperature distribution is very uniform. Ling et al. [28] compared PCM-only systems and systems that integrated PCM with forced-air convection cooling to the BTM performance. They used a battery pack surrounded by an RT44HC/expanded graphite (EG) composite with an appropriate melting temperature and high specific enthalpy, with five cells arranged in series and four parallel rows of 20 cylindrical lithium-ion batteries. According to their findings, the Tmax of the battery pack using only PCM exceeded 60 °C in two cycles.

In systems with the PCM and forced convection air cooling, the package's Tmax was successfully controlled below 50 °C in all cycles, even when the air temperature rises by 7 °C. Hemery et al. [31] developed a PCM-based BTM with an active liquid cooling system to cure the molten PCM. They built the system by installing two cooling plates with water circulation on the top and bottom of an aluminum can containing a PCM and replacing the batteries with an electric heater. Through the solidification test, the battery was quickly charged at a rate of 2C after three drive cycles, the water temperature remained unchanged at 22 °C, and the PCM was successfully cured. Although active cooling increases the complexity, the hybrid system had better thermal management capabilities, especially in harsh environments [32]. Hybrid BTMSs are still in the laboratory stage, and the amount of research on this kind of BTMS is increasing.

In this paper, three novel scheme (named scheme B, scheme C, and scheme D) BTMSs are proposed to improve the heat transfer of a conventional ACS. Scheme B introduces hollow spoiler prisms, scheme C adds PCM to a hollow spoiler prism, and scheme D introduces fins on the basis of scheme C. The cooling performances of the three improved schemes and a conventional ACS are compared by numerical simulation, using commercial computational fluid dynamics (CFD) software (Ansys-FLUENT). Their performance in preventing TR propagation is also analyzed. The paper may be conducive to the improvement of ACS.

2. Numerical Computation Methodology

2.1. Computational Domain and Boundary Conditions

In present study, the battery pack consists of several rows of 18,650 batteries. Each row contains four batteries. The battery thermophysical parameters are displayed in Table 1 [33].

Table 1. Physical and thermal properties of the 18,650 li-ion battery [33].

Rated Voltage (V)	3.6	**Specific Heat Capacity ($J \cdot kg^{-1} K^{-1}$)**	1200	**Density ($kg \cdot m^{-3}$)**	2722
Length (mm)	65	**Diameter (mm)**	18	**Anisotropic thermal conductivity ($W \cdot m^{-1} K^{-1}$)**	k_r = 0.2, k_z = 37.6

As shown in Figures 1–4, one of the rows is considered as the computational domain due to symmetrical geometry. For convenience, the batteries from the entrance to the exit are named 1, 2, 3, and 4, respectively. For the benchmark (shown in Figures 1 and 4) scheme A, the BTMS was only equipped with ACS. An improved scheme with hollow prism structures to enhance turbulence was designed as scheme B (shown in Figure 2). Filling up PCM to the hollow prisms in scheme B was designed as scheme C (also shown in Figure 2). In terms of scheme D, the aluminum fins were installed on both sides of the prism to enhance heat transfer, based on scheme C (shown in Figure 3). All of the schemes did not increase the volume of the BTMS or add additional power equips, such as pumps or fans. The commercial CFD code, ANSYS-Fluent, is applied to evaluate the performance of BTMSs with four schemes [34]. The computational domain of scheme A is Illustratively given in Figures 1 and 4. The length and width of the computational domain are 104 mm and 26 mm, respectively. The center distance between the two adjacent batteries is 26 mm. For schemes B, C, and D, the diagonal lengths (Dx and Dy) of the prism are 12 mm, as shown in Figures 2 and 3. As for scheme D, the thickness of the aluminum fins is 0.2 mm, and the height is the same as that of battery (65 mm). The influences of fin height L on heat dissipation performance will be analyzed.

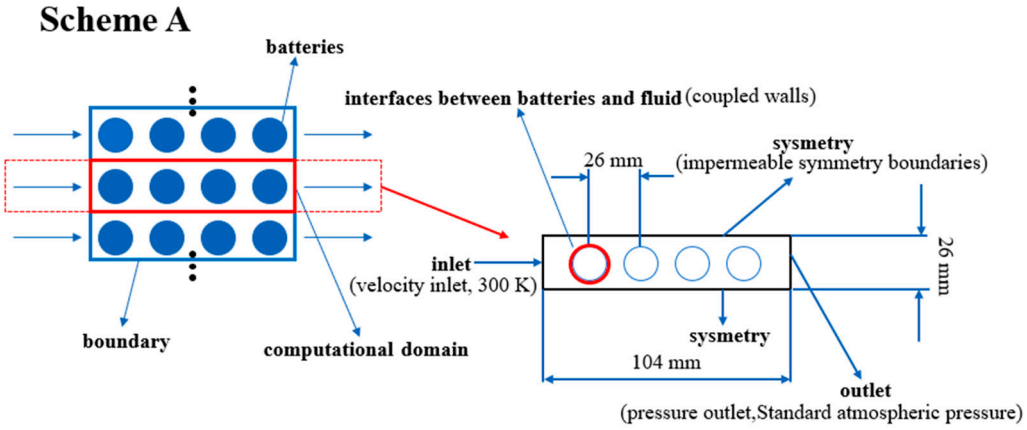

Figure 1. Benchmark scheme (scheme A) and computational domain.

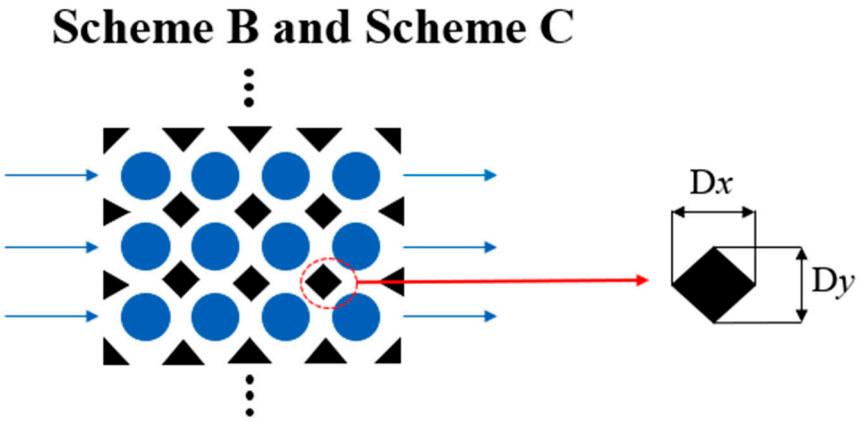

Figure 2. Spoiler prism scheme (schemes B and C).

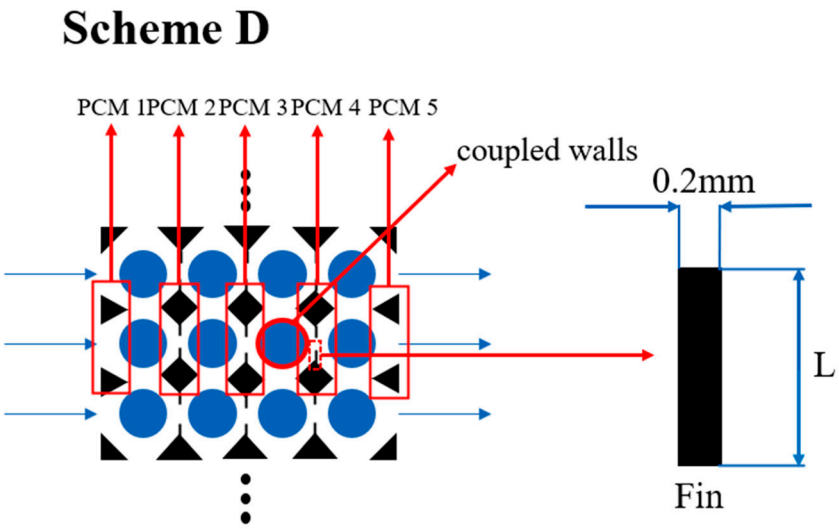

Figure 3. Outer fin scheme (scheme D).

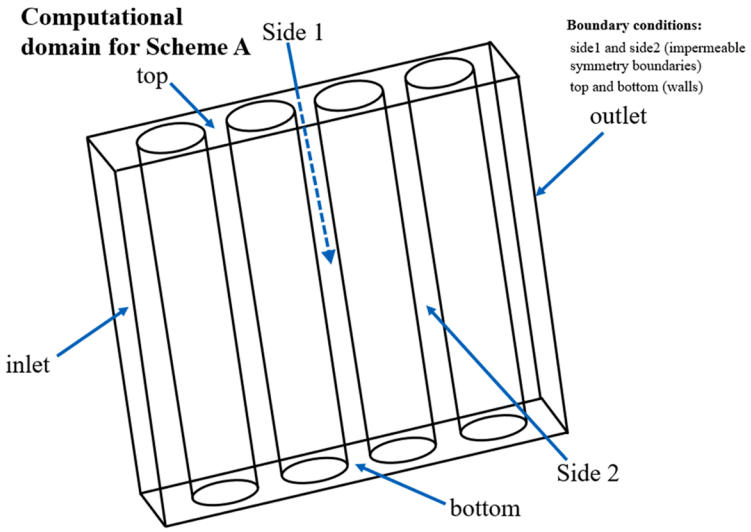

Figure 4. Computational domain for scheme A.

The settings for the boundary conditions are shown in Table 2. Six faces form the computational domain, specially (1) inlet, (2) outlet, (3) bottom, (4) top, (5) side 1, (6) side 2. The inlet and outlet are set as the velocity inlet and the pressure outlet, respectively. The top and bottom are defined as walls. Side 1 and side 2 are defined as impermeable symmetry boundaries. In addition, the interfaces between batteries and fluid are defined as coupled walls. The initial temperature is the same as the ambient temperature (300 K).

Table 2. Boundary condition settings.

Region	Inlet	Outlet	Bottom	Top	Side 1 and Side 2	Interfaces between Batteries and Fluid	Initial Temperature	Ambient Temperature
Boundary conditions	velocity inlet	pressure outlet	walls	walls	impermeable symmetry	coupled walls	300 K	300 K
Region	Inlet	Outlet	Bottom	Top	Side 1 and Side 2	Interfaces between Batteries and Fluid	Initial Temperature	Ambient Temperature
Boundary conditions	velocity inlet	pressure outlet	walls	walls	impermeable symmetry	coupled walls	300 K	300 K

2.2. CFD Model

In ANSYS-Fluent, the governing equations were discrete by the finite volume method, including the continuity, momentum, and energy equations. For the cooling air, these equations are expressed as:

Continuity equation:

$$\rho a\left(\frac{\partial}{\partial t}+\nabla\vec{v}\right)=0, \tag{1}$$

Momentum equation:

$$\frac{\partial\left(\rho a\vec{v}\right)}{\partial t}+\nabla\left(\rho a\vec{v}\vec{v}\right)=-\nabla Pa, \tag{2}$$

Energy equation:

$$\frac{\partial(\rho aCpaTa)}{\partial t} + \nabla \cdot \left(\rho aCpa\vec{v}Ta\right) = \nabla \cdot (Ka\nabla Ta), \tag{3}$$

For the battery cell, the energy governing equation is given by:

$$\rho bCpb\frac{\partial T}{\partial t} = \nabla \cdot (Kb\nabla T) + q, \tag{4}$$

where ρ, C_p, T, P, K, and q denote the density, specific heat, temperature, pressure, heat conductivity coefficient, the heat generation rate per unit volume of the battery, respectively. The subscripts a and b represent the air and battery cells, respectively.

A battery is regarded as uniform a heat source. The heat generation rate per unit volume is expressed as [35]:

$$q = \frac{1}{V}\left[I^2R_e - IT\frac{\partial U_{OCV}}{\partial T}\right], \tag{5}$$

where V is the volume of the battery; I is the current flowing through the battery; Re is the total internal resistance of the battery, including the ohmic resistance and the polarization internal resistance of the battery; T is the temperature; $UOCV$ represents the open-circuit voltage; $\frac{\partial U_{OCV}}{\partial T}$ is the entropy heat coefficient. The heat generation model is defined as an energy source term incorporated into CFD simulation using a user-defined function (UDF).

The standard k-ε model is selected which has been widely validated in modeling general low-speed and low-pressure flow around obstacles [36–39]. The $k-\varepsilon$ turbulence model includes two equations [40] for the turbulent kinetic energy k and the turbulent kinetic energy dissipation rate ε.

Turbulent kinetic energy equation:

$$\frac{\partial}{\partial t}(\rho k) + \frac{\partial}{\partial xj}(\rho kuj) = \frac{\partial}{\partial xj}\left(\left(\mu + \frac{\mu t}{\alpha k}\right)\frac{\partial k}{\partial xj}\right) + Gk + Gb - \rho\varepsilon - YM + Sk, \tag{6}$$

Turbulent kinetic energy dissipation equation:

$$\frac{\partial}{\partial t}(\rho\varepsilon) + \frac{\partial}{\partial xj}(\rho\varepsilon uj) = \frac{\partial}{\partial xj}\left(\left(\mu + \frac{\mu t}{\alpha\varepsilon}\right)\frac{\partial\varepsilon}{\partial xj}\right) + C1\varepsilon\frac{\varepsilon}{k}(Gk + C3\varepsilon Gb) - \rho C2\varepsilon\frac{\varepsilon^2}{k} + S\varepsilon, \tag{7}$$

where k and ε denote turbulent kinetic energy and turbulent dissipation rate, respectively.

2.3. Validation of CFD Model

The computational domain was discretized into unstructured grids. Grid independence tests were conducted for each scheme to ensure the accuracy of the calculation results. Battery temperatures are determined by heat generation and heat dissipation. A li-ion battery test carried out by E et al. [41] was used to validate the heat generation sub-model. More information regarding the experimental settings and parameter analysis can be found in the references [42]. A battery was discharged in a natural convection environment. The heat transfer coefficient of the battery surface was set as 5 W ($m^2 \cdot K^{-1}$) in the simulation. Figure 5 compares the simulated and measured time-varying temperatures at discharge rates = 0.5 and discharge rates = 1. In general, the CFD predicted agrees with the test results. Some deviations are caused by the inaccurate natural convection heat transfer coefficient used in the simulation and experimental errors. The simulation validation of heat dissipation can be found in our previous research in Ref. [10]. Overall, CFD technology provides high accuracy in the simulation results of battery heat generation and heat dissipation.

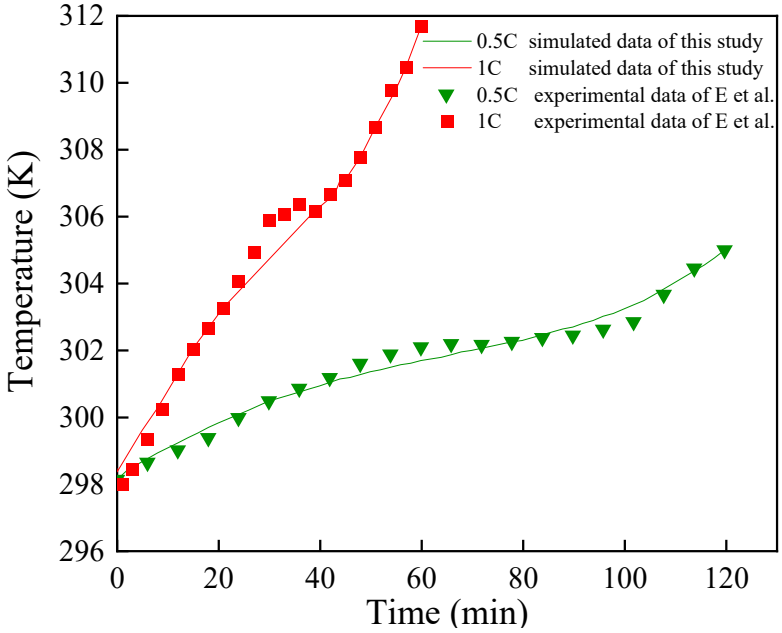

Figure 5. Heat generation model validation for a single battery. Reprinted with permission from ref. [41]. Copyright 2018, Copyright Applied Thermal Engineering.

3. Results and Discussion

The Tmax and the maximum temperature difference (ΔTmax) are the two most pivotal assessment criteria to evaluate the performance of a BTMS. The ΔTmax is defined as the maximum temperature difference between the batteries.

3.1. Computational Domain and Boundary Conditions

Figure 6 shows the temperature distribution of the middle section of the computational at different inlet air velocities at 2C discharge rates. The Tmax reduces with the rise of the inlet velocity because the convective heat transfer coefficient on the battery surface increases. However, when the inlet air velocity reaches a certain level, the effect of raising the inlet air velocity on the decreasing Tmax becomes worse. It is true that increasing the inlet velocity will raise the power consumption of the fan and then increase the operating load of the battery system. Therefore, when the ACS parameters are designed for a BTMS, an excessively high inlet velocity is not commended. At a velocity of 3.0 m/s, the temperature distribution in the middle section differs very little from the temperature distribution at a velocity of 2.5 m/s. Thus, in the present paper, the maximum inlet air velocity is 2.5 m/s.

3.2. Performance Analysis Improved Schemes

The improvement of the heat transfer of an ACS can be achieved by enhancing the turbulence and local velocity inside the pack. Several novel schemes by introducing spoiler prisms are proposed for heat transfer enhancement, as shown in Figure 2 (scheme B and scheme C). The preliminary optimization scheme (Scheme B) is that the spoiler prism is sieged with four baffles, without an increase in weight significantly owing to a hollow structure. The baffles are manufactured with 1.5 mm thick aluminum. Through the improvement of scheme B, scheme C injects the PCM into the spoiler prism. With high latent heat, the PCM can absorb substantial heat without a significant increase in temperature; therefore, the temperature uniformity may be improved. Under a TR condition, the PCM may also hinder the TR propagation by absorbing a large amount of heat.

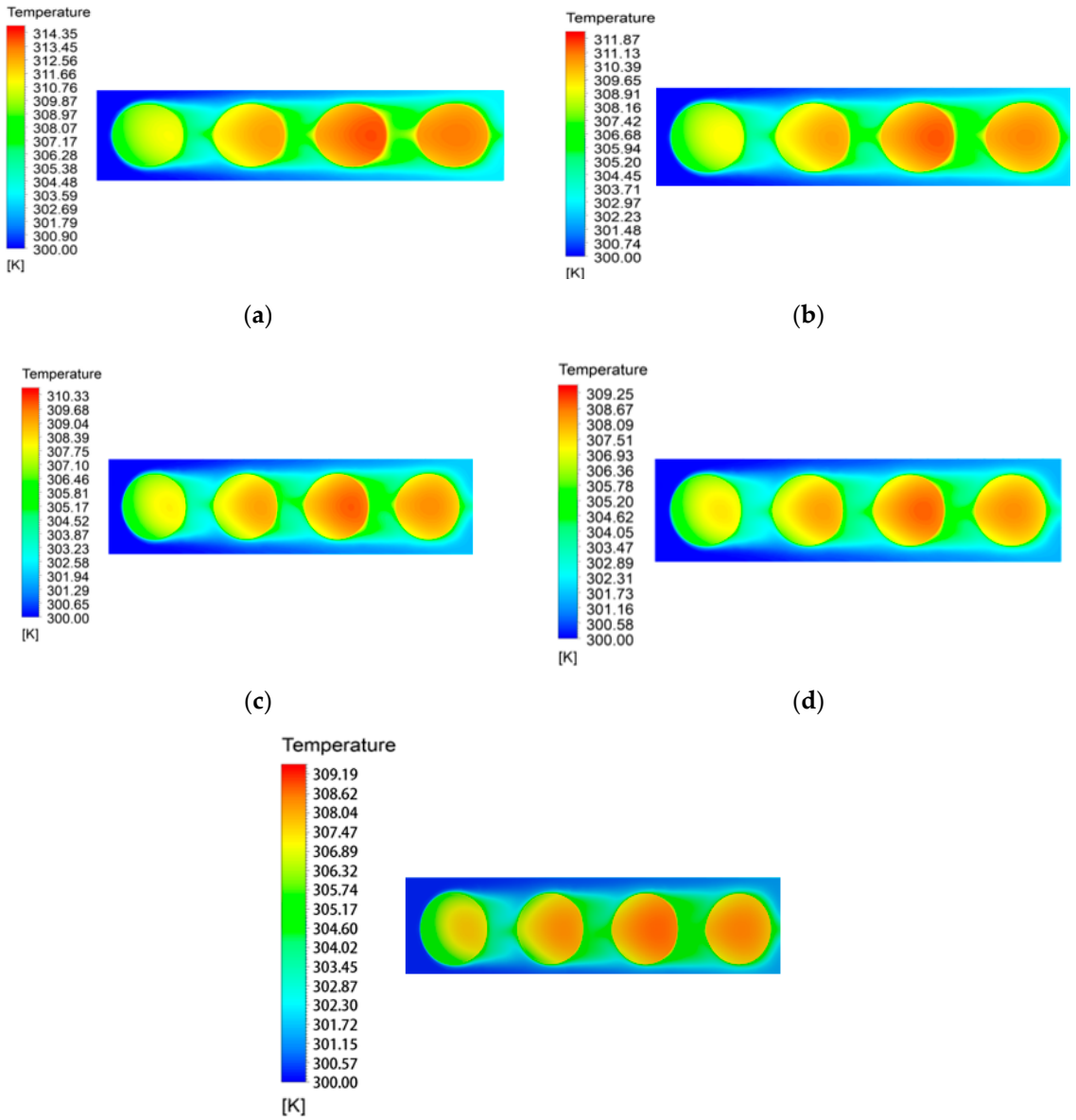

Figure 6. The temperature distribution of the middle section at different inlet velocities: (**a**) 1 ms^{-1}; (**b**) 1.5 ms^{-1}; (**c**) 2 ms^{-1}; (**d**) 2.5 ms^{-1}; (**e**) 3.0 m^{-1}.

Considering the operating temperature range during discharge, the normal octadecane-based material was selected as the PCM material. The solidus and liquidus temperatures also depend on the material purity. Based on the literature [39], the values considered for the PCM are Tsolidus = 301.15 K and Tliquidus = 303.15 K. Between these two temperatures, the PCM is considered to be in a mushy region. The variations of the specific heat are considered as a step function between these two values. In order to find the in-between values for the PCM, the values can be interpolated based on a curve fitting method. The specific heat, thermal conductivity, and density of the PCM are shown in Table 3 to be applied in the simulations [42]:

Table 3. Physical property parameters of PCMs, Reprint with permission [42].

	Specific Heat Capacity (J/kg/K)	Thermal Conductivity (W/m/K)	Density (kg/m^3)
Solid-phase PCM	2150	0.358	814
Mushy region	225,000	0.255	769
Liquid-phase PCM	2180	0.152	724

The temperature-based properties of the PCM are incorporated into the CFD simulation by a UDF. Due to the low thermal conductivity, the PCM has a significant problem of thermal inertia. Therefore, an improved type of outer fin scheme is designed, which is defined as scheme D (Figure 3). The heat dissipation capacity of the PCM is increased by adding the outer fins. Because of the good thermal conductivity of aluminum material, aluminum is used for the outer fin. The thickness of the fin is 0.2 mm, and the cooling effect of the BTMS with a fin length L of 2 mm structure is studied.

Figure 7 displays the temperature distribution in the middle section and the battery surface temperature graph at the end of the 2C discharge rates under the same temperature illustration and the 2 ms^{-1} inlet velocity under different schemes. The Tmax of the optimized schemes are significantly lower than that of the battery pack of the benchmark scheme.

Figure 8 compares, at the end of the 2C discharge rates and the 2 ms^{-1} inlet velocity, the four BTMS schemes' performances (discharge rates = 2C, Vinlet = 2 ms^{-1}). Compared to scheme A, both the Tmax and ΔTmax of the improved schemes B, C, and D decreased substantially. The Tmax of scheme D is the lowest, and the performances of schemes B and C are similar. However, scheme C introduces the PCM and is more complex than scheme B, whereas it does not enhance the performance. The performance of scheme C is inferior to that of scheme B in terms of the Tmax. Therefore, scheme C will not be discussed further.

Figure 9 demonstrates the Tmax with the inlet velocity of different batteries for discharge rates = 2C, 3C, 4C, and 5C, respectively. Specifically, the Tmax reduces with the rise of the inlet velocity, and the Tmax increases with the rise of the discharge rates. The reason is that a higher discharge rate leads to a greater heat generation rate. The Tmax of scheme B is lower than that of scheme A at four discharge rates. This is due to the addition of the spoiler prism, which improves the distribution of the flow field in the battery pack, increases the wind speed on the windward side and leeward side of the battery, and strengthens the heat transfer between the battery and the air, indicating that the spoiler prism can effectively improve the cooling performance of the battery. Moreover, as shown in Figure 9, the Tmax of scheme D decreases for scheme B at four discharge rates. This shows that the cooling effect of the BTMS can be further improved by adding outer fins. With the increase in the inlet velocity, the improvement effect of scheme D is more prominent. Taking the inlet velocity at 2 ms^{-1} as an example, the Tmax of the battery packs of different schemes increased with the increase in the discharge rates. The Tmax of scheme B decreased by 1.77 K, 2.96 K, 4.09 K, and 5.06 K, respectively, compared with scheme A, and the Tmax of scheme D decreased by 0.39 K, 0.75 K, 1.11 K, and 1.44 K, respectively. It shows that with the increase in the discharge rates, the advancement of scheme B compared with the scheme A battery pack Tmax is noticeable, and the improvement of scheme D relative to the scheme B battery pack Tmax is gradually obvious.

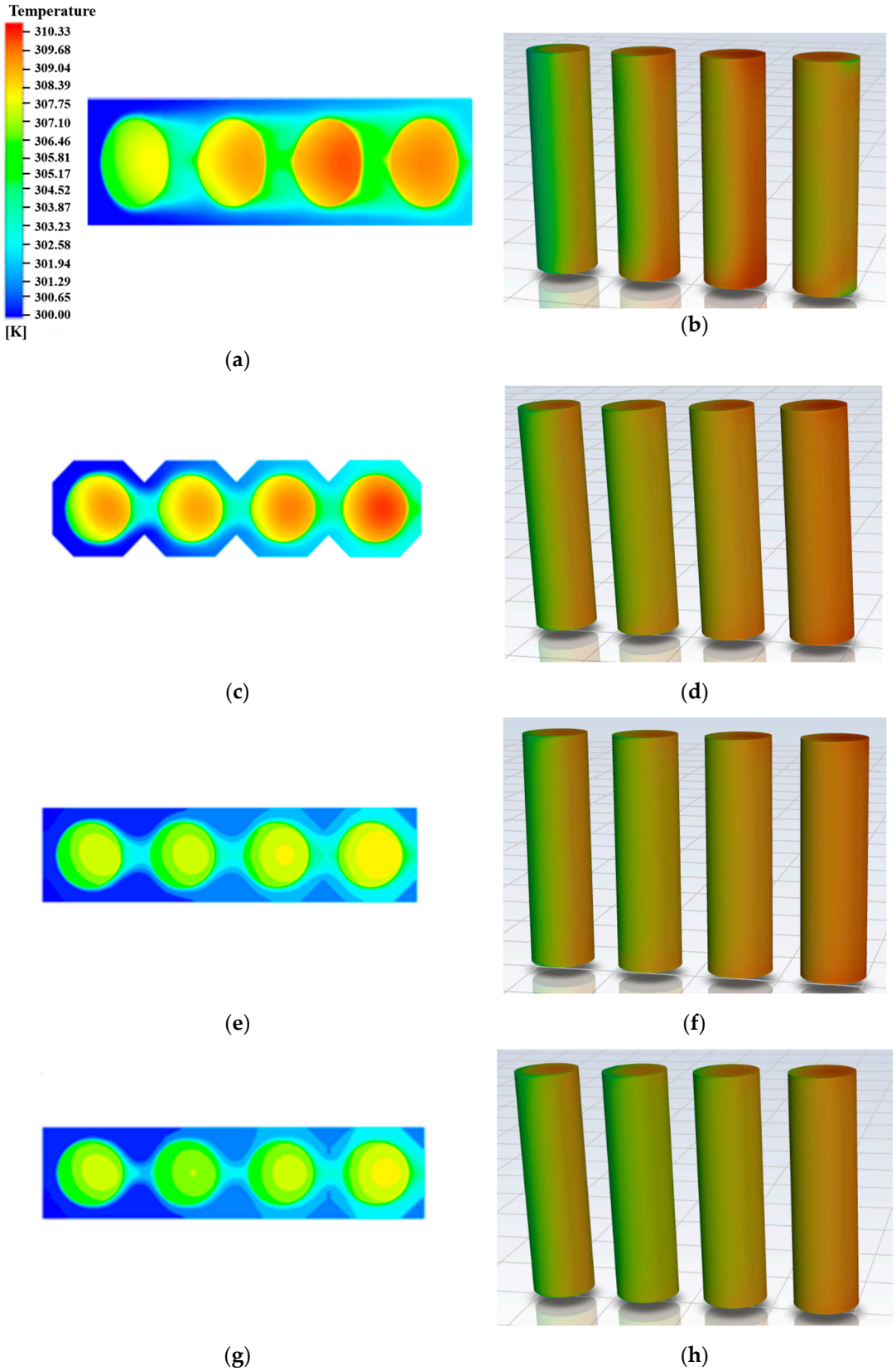

Figure 7. Temperature distribution in the middle section of different schemes and their battery surface temperature graph. (**a**) Scheme A; (**b**) the surface temperature of the battery for scheme A; (**c**) scheme B; (**d**) the surface temperature of the battery for scheme B; (**e**) scheme C; (**f**) the surface temperature of the battery for scheme C; (**g**) scheme D; (**h**) the surface temperature of the battery for scheme D.

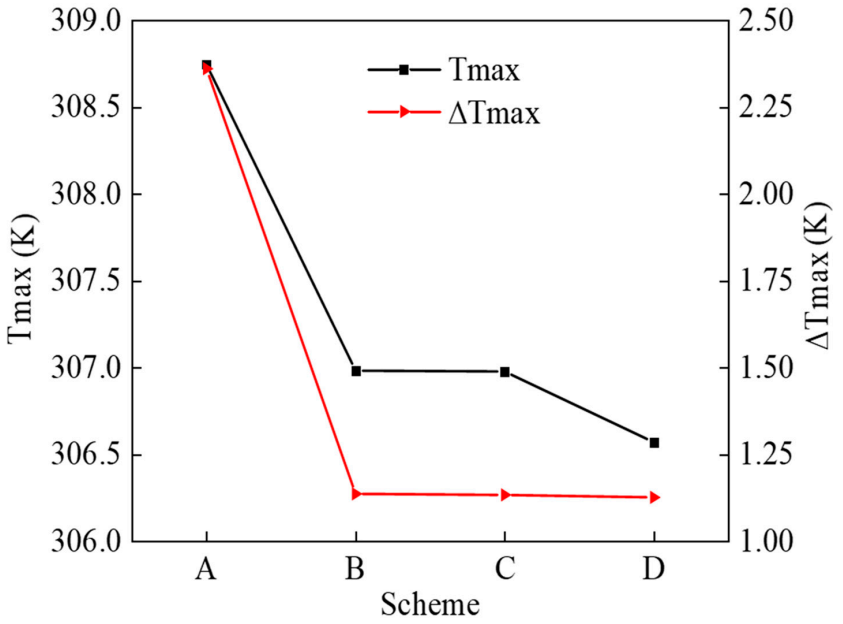

Figure 8. Tmax and ΔTmax under different schemes.

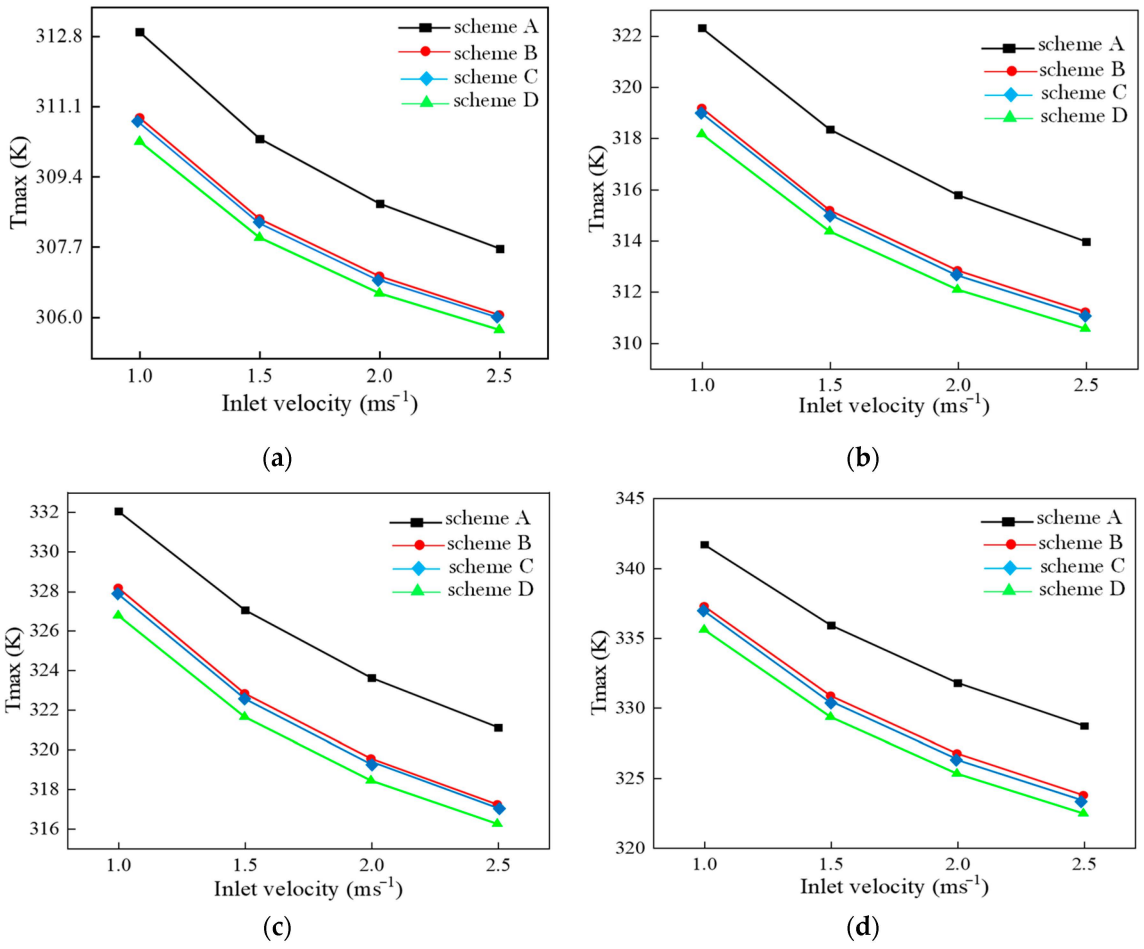

Figure 9. Variation of Tmax of scheme A, scheme B, scheme C, and scheme D with different inlet velocity. (**a**) The 2C Dr (discharge rates) discharge end; (**b**) 3C Dr discharge end; (**c**) 4C Dr discharge end; (**d**) 5C Dr discharge end.

Comparing Figures 9 and 10, the ΔTmax of the battery pack shows the same trend as that of most Tmax measurements. Under several operating conditions, the ΔTmax decreases with the increase in the air inlet velocity, because the increase in the inlet velocity strengthens the convective heat transfer between the battery and the air, which makes the temperature distribution of the battery pack more uniform. Therefore, considering the energy consumption of the system, the inlet velocity can be appropriately increased to enhance the temperature uniformity of the battery pack. Moreover, as shown in Figure 10, at the same discharge rates, the ΔTmax of scheme B decreases relative to that of scheme A, and that of scheme D decreases when the inlet velocity is less than 2 ms^{-1}, indicating that the addition of fins can enhance the temperature uniformity when the inlet velocity is less than 2 ms^{-1}. However, when the inlet velocity is greater than 2 ms^{-1}, with the increase in the inlet velocity, the maximum temperature difference in the battery pack with scheme D is gradually larger than that of scheme B, which is mainly due to the decrease in the airflow channel between the two adjacent batteries due to the addition of the fins. The upwind area of the battery will also decrease, and the forced convection heat transfer area between the battery and air will decrease, resulting in an uneven heat transfer and worse temperature uniformity in the whole battery pack.

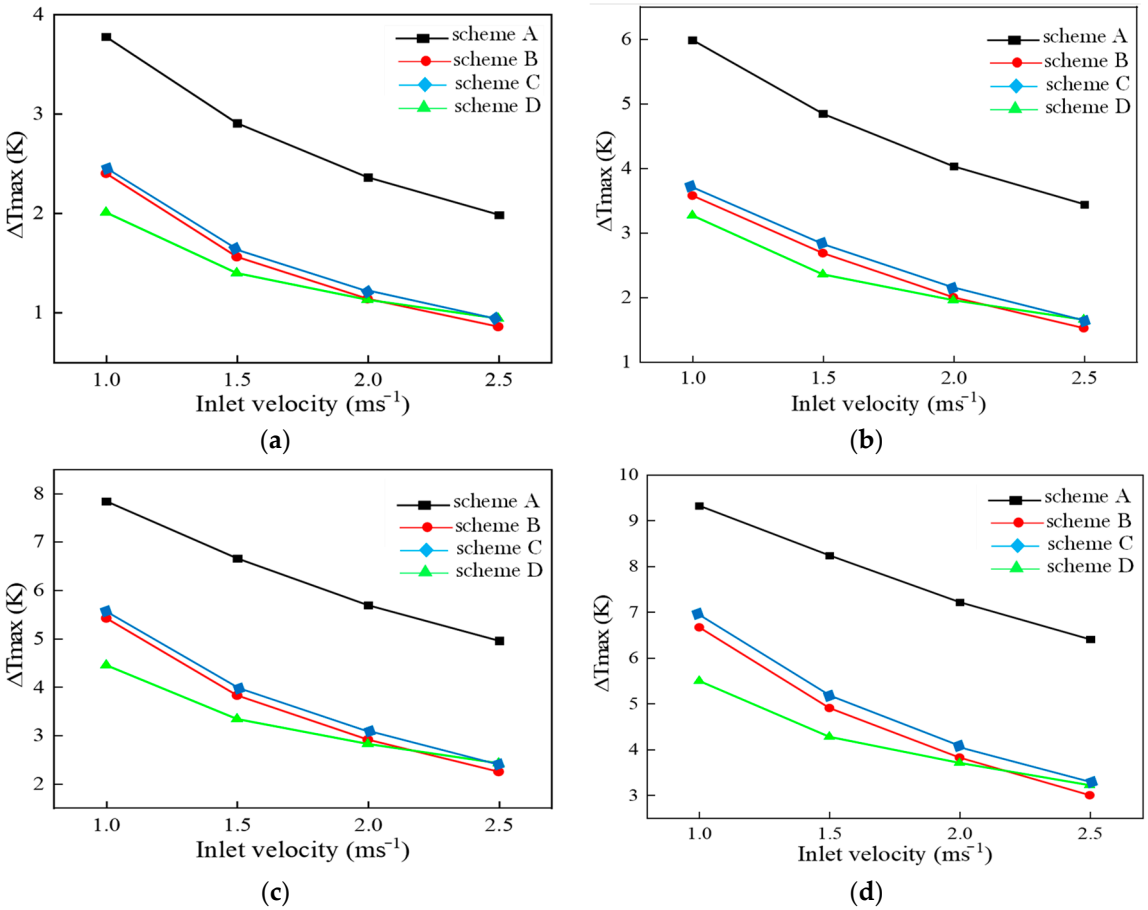

Figure 10. Variation of ΔTmax of scheme A, scheme B, and scheme D with inlet velocity. (**a**) The 2C Dr (discharge rates) discharge end; (**b**) 3C Dr discharge end; (**c**) 4C Dr discharge end; (**d**) 5C Dr discharge end.

4. Performance under TR Condition

When a battery triggers the TR in a pack, the heat generated will spread to the adjacent battery and may lead to the propagation of the TR [43]. During the TR, the energy released by a single battery is relatively limited, but the TR propagation may release all the energy stored in the battery pack, resulting in more serious risk. If the heat flow spreads

throughout the battery pack, the energy contained in the high-density battery pack may cause significant damage to the surrounding objects and people [44]. Therefore, the security design for the TR spread suppression is essential.

Different from establishing a conventional battery TR model, there is a relatively extreme definition of a fully charged li-ion battery that releases all its energy in the form of heat within 10 s. According to the capacity, nominal voltage, and volume of the li-ion battery, Shen et al. [45] calculated that the heat generation rate of a li-ion battery is about 120 MW m^{-3} in the case of prescribed TR.

In this paper, the heat source value of the same order of magnitude is simulated to approximately represent the heat source value of the general TR condition. When the Tmax exceeds the threshold (423 K), the battery TR is triggered [46]. The No. 1 battery and the No. 2 battery are assumed to occur TR, respectively. The TR and heat transfer of the battery are studied by monitoring the maximum temperature of the battery. Before demonstrating the performance of the PCM in a TR state, it is assumed that the battery pack runs at a discharge rate of 1C in the first 60 s, and then the designated No. 1 and No. 2 batteries are thermally out of control for 10 s. The remaining batteries remain in normal operation throughout the process. At the same time, the cooling air controls the battery temperature at the inlet velocity of 1 ms^{-1}, and the process lasts 500 s.

When TR occurs, the battery temperature rises dramatically. Consequently, the temperature difference between the battery with TR and its adjacent battery tends to be extremely large. Thus, the radiation heat transfer will dominate. The surface-to-surface (S2S) radiation model is applied to account for the radiation exchange in an enclosure of gray-diffuse surfaces in this simulation. The energy exchange between two surfaces depends in part on their size, separation distance, and orientation. These parameters are accounted for by a geometric function called a "view factor". The main assumption of the S2S model is that any absorption, emission, or scattering of radiation can be ignored; therefore, only "surface-to-surface" radiation need be considered for the analysis. The energy flux leaving a given surface is composed of directly emitted and reflected energy:

$q_{out,k} = \varepsilon_k \sigma T^4 + \rho_k q_{in,k}$ where $q_{out,k}$ is the energy flux leaving the surface, ε_k is the emissivity, σ is Boltzmann's constant, and $q_{in,k}$ is the energy flux incident on the surface from the surroundings.

Figure 11 shows the change in the maximum temperature of each battery in the pack with time when the No. 1 battery triggers the TR. At 60 s, the temperature of the No. 1 battery suddenly rises to 956.61 K, and then the TR spreads to the adjacent battery. When the system runs to 140 s, the Tmax of the No. 2 battery reaches 423.11 K, which exceeds the threshold of the maximum temperature of the TR (423 K), and triggers the TR of the No. 2 battery, which also lasts for 10 s. When the system runs to 169 s, the Tmax of the No. 3 battery is 424.79 K, which exceeds 423 K, and the TR lasts for 10 s. When the system runs to 193 s, the Tmax of the No. 4 battery is 424.32 K, which is also out of control, and the system continues to run until 500 s. As shown in Figure 11, the time interval between the TR of the No. 1 battery and the TR of the No. 2 battery is 80 s. The time between the TR of the No. 2 battery and the TR of the No. 3 battery is 29 s, and the interval between the TR of the No. 3 battery and the TR of the No. 4 battery is 24 s. It can be seen that the time interval of the TR between the two adjacent batteries becomes smaller and smaller. In addition, the Tmax of the No. 2, No. 3, and No. 4 batteries are 1046.68 K, 1047.29 K, and 1051.91 K, respectively. Except for the relatively low Tmax of the No. 1 battery, the Tmax of the other batteries is almost the same. This is because when the No. 1 battery is out of control, the temperature of the other three batteries is also gradually rising. By analogy, the No. 4 battery closest to the exit has the shortest time to get out of control, and the No. 1 battery has the lowest Tmax.

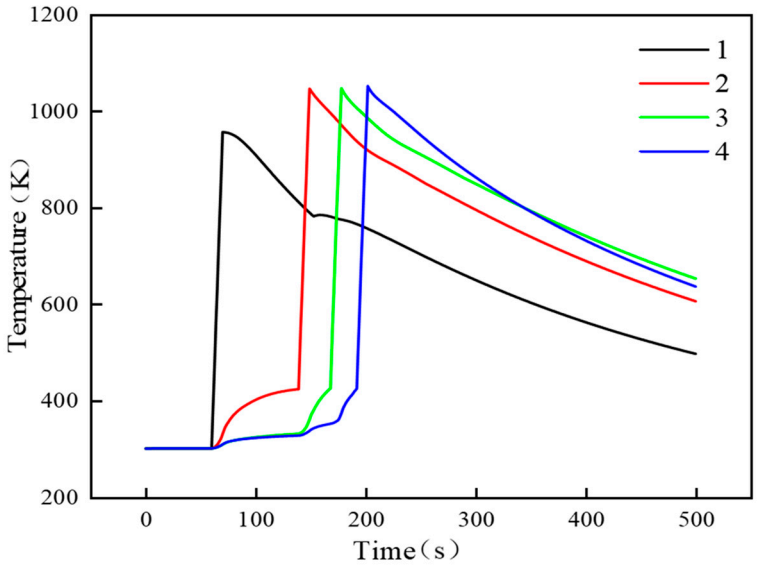

Figure 11. The maximum body temperature of each battery in scheme A under the condition of TR (when setting No. 1 battery TR).

Figure 12 shows the Tmax changes in each battery in scheme D under the condition of TR. It can be seen that, except for the TR of the No. 1 battery, the other batteries are not out of control. The Tmax of the No. 1 battery reaches 694.62 K 10 s after the TR occurs. Among them, the Tmax of the No. 2 battery appeared when the system was running for 122 s, and the Tmax was 353.11 K, which did not reach the maximum temperature of the TR threshold. Finally, the temperature of the No. 2 battery began to decrease gradually. The Tmax of the No. 3 battery appears when the system runs for 184 s, and the Tmax is 323.57 K. The Tmax of the No. 4 battery appears when the system runs for 211 s, and the Tmax is 320.58 K. After running the PCM-based BTMS, the No. 1 battery still exceeds the temperature threshold. Although the TR of a single battery is not effectively suppressed, it can prevent the TR from spreading from a single battery to the adjacent battery. The Tmax of the No. 2, No. 3, and No. 4 batteries is lower than the critical temperature of the TR, which indicates that the use of PCMs and fin interception can effectively reduce the battery temperature and make the heat generated by the battery be absorbed by the latent heat of the PCMs. The latent heat of the PCM is used to store the heat generated by the battery, and a forced ACS can take away the latent heat to prevent heat accumulation.

Figure 13 shows the change in the maximum temperature of each battery in the battery pack with time when the No. 2 battery is out of control. At 60 s, the temperature of the No. 2 battery suddenly rises to 961.38 K, and then the TR spreads to the adjacent battery. The Tmaxs of both the No. 1 battery and NO. 3 battery exceed the threshold of the maximum temperature of the TR (423 K) and triggers the TR propagation. When the system runs to 190 s, the Tmax of the No. 4 battery produces the TR as well, mainly due to the heat from the No. 3 battery. As shown in Figure 11, the time interval between the TR of the No. 2 battery and the TR of the No. 1 battery is 80 s. The time between the TR of the No. 1 battery and the TR of the No. 3 battery is 15 s, and the interval between the TR of the No. 3 battery and the TR of the No. 4 battery is 35 s. It can be seen that the TR interval between the No. 1 and No. 2 batteries is the shortest. In addition, the Tmax of the No. 1, No. 3, and No. 4 batteries are 986.31 K, 992.47 K, and 1050.91 K, respectively. This is because the No. 2 battery is a TR battery, and its heat is emitted to both sides. The heat dissipated diffuses to both the No. 1 battery and the No. 3 battery at the same time and, finally, to the No. 4 battery.

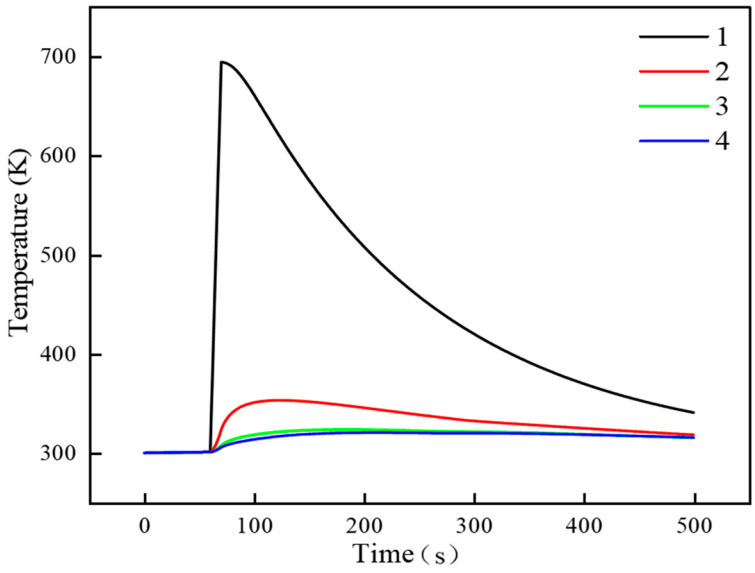

Figure 12. The maximum body temperature of each battery in scheme D under TR (when considering No. 1 battery TR).

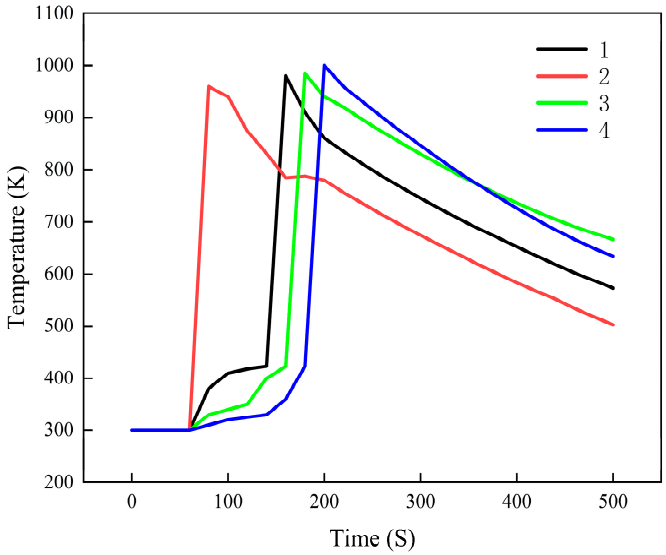

Figure 13. The maximum body temperature of each battery in scheme A under the condition of TR (when setting No. 2 battery TR).

Figure 14 shows the Tmax changes in each battery in scheme D under the condition of TR (when setting the No. 2 battery TR). It can be seen that, except for the TR of the No. 2 battery, the other batteries are not out of control. The Tmax of the No. 1 battery reaches 689.53 K 10 s after the TR occurs. Among them, the Tmax of the No. 1 battery appeared when the system was running for 120 s, and the Tmax was 343.22 K, which did not reach the maximum temperature of the TR threshold. Finally, the temperature of the No. 1 battery began to decrease gradually. The Tmax of the No. 3 battery appears when the system runs for 120 s, and the Tmax is 332.48 K. The Tmax of the No. 4 battery appears when the system runs for 205 s, and the Tmax is 318.66 K. After running the PCM-based BTMS, the No. 2 battery still exceeds the temperature threshold. It can be seen that setting the No. 2 battery to a TR battery does not cause TR for the other batteries as well as setting the No. 1 battery to a TR battery.

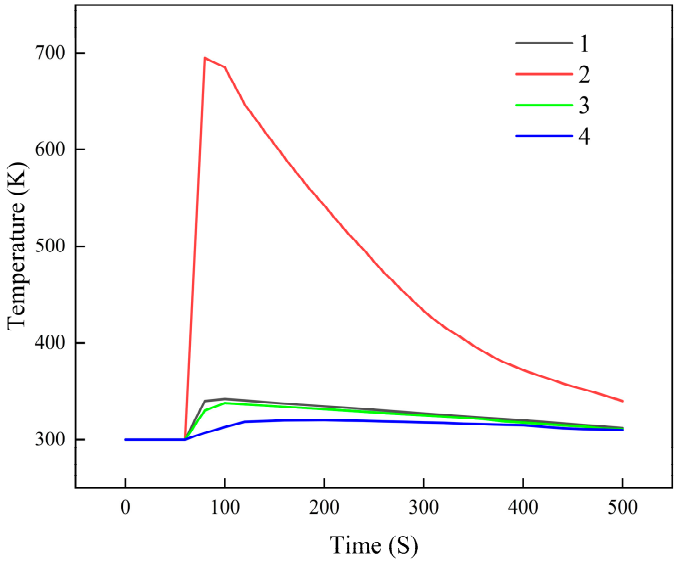

Figure 14. The maximum body temperature of each battery in model d under TR (when setting No. 2 battery TR).

When TR occurs, a large amount of heat generated by the battery is absorbed by the PCM, and because the PCM is a phase-change material, it can maintain its own temperature without major changes when absorbing or releasing a large amount of heat. Because the temperature of the PCM is hardly raised, heat is not radiated to adjacent batteries so that the TR of the effective tissue propagates between the cells.

We can see from Figure 15 that when the No. 1 battery is designated as a thermally runaway battery (the locations of the different PCMs are shown in Figure 3), PCM1 and PCM2 adjacent to the No. 1 batteries are relatively high in temperature. The maximum temperature of PCM1 reached 302.31 K, and the maximum temperature of PCM2 reached 301.98 K. Then, the farther away from the No. 1 battery, the PCM temperature will be lower, and the maximum temperature of PCM3 was 301.75 K, PCM4 was 301.63 K, and PCM5 was 301.38 K.

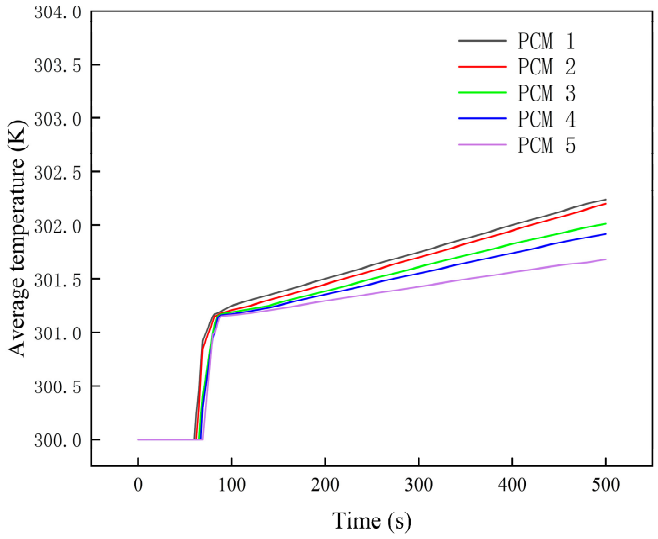

Figure 15. The average temperature change in the PCM in different regions when the No. 1 battery is thermally runaway.

Figure 16 shows the average temperature change in each PCM when the No. 2 battery is a TR battery. Because PCM2 and PCM3 are close to the No. 2 batteries, their temperatures

are relatively high. Their average temperatures reached a maximum of 302.41 K and 302.33 K. The rest of the PCM is far away from the No. 2 battery and has a relatively low average temperature, and the average temperature of PCM1 reached a maximum of 301.88 K, PCM4 was 301.71 K, and PCM5 was 301.42 K.

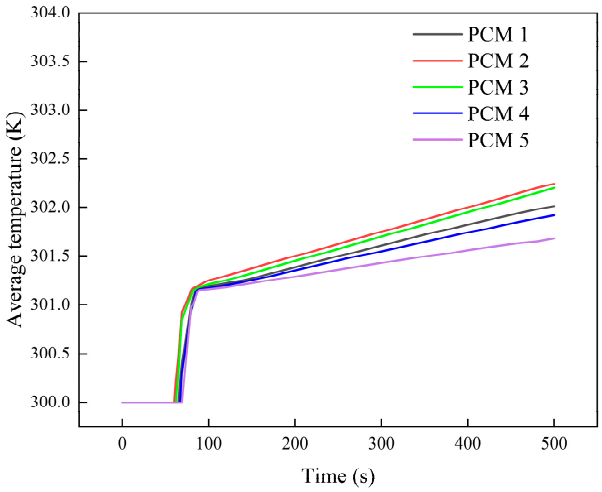

Figure 16. The average temperature change in the PCM in different regions when the No. 2 battery is thermally runaway.

The Table 4 shows the range/value of the inputs. We can see from the table that the inlet velocity speed is 0 m/s. This is because, under the TR conditions, the fans are all turned off.

Table 4. The range/value of inputs.

Heat Generation Rate	**Inlet Velocity**	**Outlet Velocity**	**Inlet Boundary Conditions**	**Outlet Boundary Conditions**	**Radiation Model**
120 MW m^{-3}	**0 m/s**	**0 m/s**	Velocity inlet	Pressure out	S2S
Top and bottom boundary conditions	**Side1 and Side2 boundary conditions**	**Initial temperature**	**Ambient temperature**	**Interfaces**	
wall	Impermeable symmetry	300 K	300 K	Coupled walls	
Heat Generation Rate	**Inlet Velocity**	**Outlet Velocity**	**Inlet Boundary Conditions**	**Outlet Boundary Conditions**	**Radiation Model**
120 MW m^{-3}	0 m/s	0 m/s	Velocity inlet	Pressure out	S2S
Top and bottom boundary conditions	**Side1 and Side2 boundary conditions**	**Initial temperature**	**Ambient temperature**	**Interfaces**	
wall	Impermeable symmetry	300 K	300 K	Coupled walls	

Table 5 shows the range/value of outlets.

Table 5. The range/value of outlets.

The Maximum Temperature of Scheme A under TR	**No. 1**	**No. 2**	**No. 3**	**No. 3**
	956.61 K	1046.68 K	1047.29 K	1051.91 K
The Maximum Temperature of Scheme D under TR	**No. 1**	**No. 2**	**No. 3**	**No. 3**
	694.62 K	353.11 K	323.57 K	320.58 K

From the above data, it can be seen that the TR of scheme A will be propagated, while the TR of scheme D will not propagate.

5. Conclusions

In this paper, the scheme of the aligned battery pack is improved, and the temperature distribution in the battery pack of different schemes is compared by adding a spoiler prism, the PCM, and an outer fin. The maximum temperature and maximum temperature difference in the battery pack under different design schemes are calculated and compared. The results show that:

(1) Under the different schemes, the Tmax and ΔTmax of the battery pack decrease with the increase in the inlet velocity, and the Tmax and ΔTmax of the battery pack increase with the increase in the discharge rates at a fixed inlet velocity.
(2) The performance of an ACS BTMS can be improved by introducing a hollow prismatic turbulence structure. Its performance can be further enhanced by filling PCM in the hollow prismatic spoiler structure and adding fins.
(3) The optimization scheme D can effectively prevent the TR propagation between batteries.

This article can be used for the study of adding prism structures and fins to battery modules. Without increasing the volume of the BTMS or adding additional power equipment, a better reduction in battery temperature is achieved, providing a feasible method for improving the performance of an air-cooled thermal battery management system. The limitation of this article is that the TR of the design is relatively rough and does not take into account the problem of damage or leakage caused by the impact of the unit. Potential future work will be directed to: (i) study the heat dissipation of the battery module by changing the material and size of the fins and (ii) consider the problem of leakage after the battery cell receives a solid impact.

Author Contributions: Methodology, W.C.; data curation, W.C. and X.L.; resources, S.H. and P.H.; software, S.H.; supervision, J.S. and B.W.; validation, J.S.; project administration, P.H.; writing—original draft, B.L.; writing—review and editing, B.L.; visualization, B.W.; formal analysis, X.L. All authors have read and agreed to the published version of the manuscript.

Funding: This research was funded by [Hebei province administrated Universities] grant number [ZCT202002] And The APC was funded by [ZD2019015]. Fundamental research fund for Hebei province administrated Universities (ZCT202002); Hebei Provincial Department of Education Funded Scientific Research Project (ZD2019015).

Institutional Review Board Statement: Not applicable.

Informed Consent Statement: Not applicable.

Data Availability Statement: Not applicable.

Conflicts of Interest: The authors declare no conflict of interest.

References

1. Luna, T.F.; Uriona-Maldonado, M.; Silva, M.E.; Vaz, C.R. The influence of e-carsharing schemes on electric vehicle adoption and carbon emissions: An emerging economy study. *Transp. Res. Part D Transp.* **2020**, *79*, 102226. [CrossRef]
2. Liu, H.; Wei, Z.; He, W.; Zhao, J. Thermal issues about Li-ion batteries and recent progress in battery thermal management systems: A review. *Energy Convers. Manag.* **2017**, *150*, 304–330. [CrossRef]
3. Takami, N.; Inagaki, H.; Tatebayashi, Y.; Saruwatari, H.; Honda, K.; Egusa, S. High-power and long-life lithium-ion batteries using lithium titanium oxide anode for automotive and stationary power applications. *J. Power Sources* **2013**, *244*, 469–475. [CrossRef]
4. Wilke, S.; Schweitzer, B.; Khateeb, S.; Al-Hallaj, S. Preventing TR propagation in lithium ion battery packs using a phase change composite material: An experimental study. *J. Power Sources* **2017**, *340*, 51–59. [CrossRef]
5. Lu, L.; Han, X.; Li, J.; Hua, J.; Ouyang, M. A review on the key issues for lithium-ion battery management in electric vehicles. *J. Power Sources* **2013**, *226*, 272–288. [CrossRef]
6. Fan, L.; Khodadadi, J.M.; Pesaran, A.A. A parametric study on thermal management of an air-cooled lithium-ion battery module for plug-in hybrid electric vehicles. *J. Power Sources* **2013**, *238*, 301–312. [CrossRef]

7. Panchal, S.; Khasow, R.; Dincer, I.; Agelin-Chaab, M.; Fraser, R.; Fowler, M. Thermal design and simulation of mini-channel cold plate for water cooled large sized prismatic lithium-ion battery. *Appl. Therm. Eng.* **2017**, *122*, 80–90. [CrossRef]
8. Rao, Z.; Wang, S. A review of power battery thermal energy management. *Renew. Sustain. Energy Rev.* **2011**, *15*, 4554–4571. [CrossRef]
9. Putra, N.; Ariantara, B.; Pamungkas, R.A. Experimental investigation on performance of lithium-ion battery thermal management system using flat plate loop heat pipe for electric vehicle application. *Appl. Therm. Eng.* **2016**, *99*, 784–789. [CrossRef]
10. Zhao, G.; Wang, X.L.; Michael, N.; Zhang, H.Y. A review of air-cooling battery thermal management systems for electric and hybrid electric vehicles. *J. Power Sources* **2021**, *501*, 230001. [CrossRef]
11. Wang, Y.S.; Liu, B.; Han, P. Optimization of an air-based thermal management system for lithium-ion battery packs. *J. Energy Storage* **2021**, *44*, 103314. [CrossRef]
12. Park, S.; Jung, D. Battery cell arrangement and heat transfer fluid effects on the parasitic power consumption and the cell temperature distribution in a hybrid electric vehicle. *Power Sources* **2013**, *227*, 191–198. [CrossRef]
13. Kausthubharam, P.K.; Chandrasekaran, N. Numerical investigation of cooling performance of a novel air-cooled thermal management system for cylindrical Li-ion battery module. *Appl. Therm. Eng.* **2021**, *193*, 116961. [CrossRef]
14. Li, X.X.; He, F.Q.; Zhang, G.Q.; Huang, Q.Q.; Zhou, D.Q. Experiment and simulation for pouch battery with silica cooling plates and copper mesh based air cooling thermal management system. *Appl. Therm. Eng.* **2019**, *146*, 866–880. [CrossRef]
15. Liu, Y.; Zhang, J. Design a J-type air-based battery thermal management system through surrogate-based optimization. *Appl. Energy* **2019**, *252*, 113426. [CrossRef]
16. Sheng, L.; Zhang, H.; Su, L.; Zhang, Z.D.; Zhang, H. Effect analysis on thermal profile management of a cylindrical lithium-ion battery utilizing a cellular liquid cooling jacket. *Energy* **2021**, *220*, 119725. [CrossRef]
17. Hekmat, S.; Bamdezh, M.A.; Molaeimanesh, G.R. Hybrid thermal management for achieving extremely uniform temperature distribution in a lithium battery module with phase change material and liquid cooling channel. *J. Energy Storage* **2022**, *50*, 104272. [CrossRef]
18. Hallaj, S.A.; Selman, J.R. A Novel Thermal Management System for Electric Vehicle Batteries Using Phase-Change Material. *J. Electrochem. Soc.* **2019**, *147*, 3231–3454. [CrossRef]
19. Yan, J.; Li, K.; Chen, H.; Wang, Q.; Sun, J. Experimental study on the application of phase change material in the dynamic cycling of battery pack system. *Energy Convers. Manag.* **2016**, *128*, 12–19. [CrossRef]
20. Kizilel, R.; Lateef, A.; Sabbah, R.; Farid, M.M.; Selman, J.R.; Hallaj, A.S. Passive control of temperature excursion and uniformity in high-energy Li-ion battery packs at high current and ambient temperature. *J. Power Sources* **2008**, *183*, 370–375. [CrossRef]
21. Pushpitha, V.S.; Debangsu, B. Thermal management of a high temperature sodium sulphur battery stack. *Int. J. Heat Mass Transf.* **2021**, *181*, 122025.
22. Zhao, C.Y.; Zhang, B.; Yuanming, Z.; Huang, S.Y.; Yan, T.T.; Liu, X.F. Hybrid Battery Thermal Management System in Electrical Vehicles: A Review. *Energies* **2020**, *13*, 6257. [CrossRef]
23. Ping, P.; Peng, R.; Kong, D.; Chen, G.; Wen, J. Investigation on thermal management performance of PCM-fin structure for Li-ion battery module in high-temperature environment. *Energy Convers. Manag.* **2018**, *176*, 131–146. [CrossRef]
24. Patel, J.R.; Manish, K.R. Recent developments in the passive and hybrid thermal management techniques of lithium-ion batteries. *J. Power Sources* **2020**, *480*, 228820. [CrossRef]
25. Sun, Z.; Fan, R.; Yan, F.; Zhou, T.; Zheng, N.B. Thermal management of the lithium-ion battery by the composite PCM-Fin structures. *Int. J. Heat Mass Transf.* **2019**, *145*, 118739. [CrossRef]
26. Jiaqiang, E.; Yi, F.; Li, W.J.; Zhang, B.; Zou, H.Y. Effect analysis on heat dissipation performance enhancement of a lithium-ion-battery pack with heat pipe for central and southern regions in China. *Energy* **2021**, *226*, 120336.
27. Sabbah, R.; Kizilel, R.; Selman, J.R.; Hallaj, S.A. Active (air-cooled) vs. passive (phase change material) thermal management of high power lithium-ion packs: Limitation of temperature rise and uniformity of temperature distribution. *J. Power Sources* **2008**, *182*, 630–638. [CrossRef]
28. Ling, Z.; Wang, F.; Fang, X.; Gao, X.; Zhang, Z. A hybrid thermal management system for lithium ion batteries combining phase change materials with forced-aircooling. *Appl. Energy* **2015**, *148*, 403–409. [CrossRef]
29. Kizilel, R.; Sabbah, R.; Selman, J.R.; Hallaj, S.A. An alternative cooling system to enhance the safety of Li-ion battery packs. *Power Sources* **2009**, *194*, 1105–1112. [CrossRef]
30. Mao-Sung, W.; Liu, K.H.; Wang, Y.Y.; Wang, C.C. Heat dissipation design for lithium-ion batteries. *Power Sources* **2022**, *109*, 160–166.
31. Hémery, C.V.; Pra, F.; Robin, J.F.; Marty, P. Experimental performances of a battery thermal management system using a phase change material. *Power Sources* **2014**, *270*, 349–358. [CrossRef]
32. Chen, J.W.; Kang, S.Y.; Jiaqiang, E.; Huang, Z.H.; Wei, K.X.; Zhang, B.; Zhou, H.; Deng, Y.W.; Zhang, F.; Liao, G.L. Effects of different phase change material thermal management strategies on the cooling performance of the power lithium ion batteries: A review. *J. Power Sources* **2019**, *442*, 227228. [CrossRef]
33. Behi, H.; Karimi, D.; Behi, M.; Ghanbarpour, M.; Jaguemont, J.; Sokkeh, M.A.; Gandoman, F.H.; Berecibar, M.; Mierlo, J.V. A new concept of thermal management system in Li-ion battery using air cooling and heat pipe for electric vehicles. *Appl. Therm. Eng. 2020 174*, 115280. [CrossRef]

34. *Fluent Announces First International CFD Conference Dedicated to the Oil & Gas Industry*; Fluent Europe Ltd.: Sheffield, UK, 2006; Available online: https://www.cfd-online.com (accessed on 18 June 2022).
35. Jeon, D.H.; Baek, S.M. Thermal modeling of cylindrical lithium ion battery during discharge cycle. *Energy Convers. Manag.* **2011**, *52*, 2973–2981. [CrossRef]
36. Kiˇsa, M.; Jelemenský, L. CFD dispersion modelling for emergency preparadnes. *Loss Prev. Process Ind.* **2009**, *22*, 97–104.
37. Scargiali, F.; Grisafi, F.; Busciglio, A.; Brucato, A. Modeling and simulation of dense cloud dispersion in urban areas by means of computational fluid dynamics. *J. Hazard. Mater.* **2011**, *197*, 285–293. [CrossRef]
38. Sini, J.F.; Anquetin, S.; Mestayer, P.G. Pollutant dispersion and thermal effects in urban street canyons. *Atmos. Environ.* **1996**, *30*, 2659–2677. [CrossRef]
39. Xing, J.; Liu, Z.; Huang, P.; Feng, C.; Zhou, Y.; Zhang, D.; Wang, F. Experimental and numerical study of the dispersion of carbon dioxide plume. *J. Hazard. Mater.* **2013**, *256–257*, 40–48. [CrossRef]
40. Zhang, F.; Lin, A.; Wang, P.; Liu, p. Optimization design of a parallel air-cooled battery thermal management system with spoilers. *Appl. Therm. Eng.* **2021**, *182*, 116062. [CrossRef]
41. Jiaqiang, E.; Yue, M.; Chen, J.; Zhu, H.; Deng, Y.; Zhu, Y.; Zhang, F.; Wen, M.; Zhang, B.; Kang, S. Effects of the different air cooling strategies on cooling performance of a lithium-ion battery module with baffle. *Appl. Therm. Eng.* **2018**, *144*, 231–241.
42. Javani, N.; Dincer, I. Heat transfer and thermal management with PCMs in a Li-ion battery cell for electric vehicles. *Int. J. Heat Mass Transf.* **2014**, *72*, 690–703. [CrossRef]
43. Lamb, J.; Orendorff, C.J.; Orendorff; Steele, L.A.M.; Spangler, S.W. Failure propagation in multi-cell lithium ion batteries. *J. Power Sources* **2015**, *283*, 517–523. [CrossRef]
44. Zhang, X.; Liu, C.Z.; Rao, Z.H. Experimental investigation on thermal management performance of electric vehicle power battery using composite phase change material. *J. Clean. Prod.* **2018**, *201*, 916–924. [CrossRef]
45. Shen, M.; Gao, Q. Structure design and effect analysis on refrigerant cooling enhancement of battery thermal management system for electric vehicles. *J. Energy Storage* **2020**, *32*, 101940. [CrossRef]
46. Yeow, K.; Ho, T. Characterizing Thermal Runaway of Lithium-ion Cells in a Battery System Using Finite Element Analysis Approach. *J. Altern. Powertrains* **2013**, *2*, 179–186. [CrossRef]